Atmospheric
Chemistry
and Physics
Discussions

Open Access

EGU

1 **Different effects of anthropogenic emissions and aging processes on the**

2 **mixing state of soot particles in the nucleation and accumulation**

3 **modes**

4

5 Yuying Wang[1,2], Rong Hu[1,2], Qiuyan Wang[1], Zhanqing Li[3], Maureen Cribb[3], Yele Sun[4], Xiaorui

6 Song[1], Yi Shang[1], Yixuan Wu[1], Xin Huang[1], Yuxiang Wang[1]

7

8 [1] Key Laboratory for Aerosol-Cloud-Precipitation of China Meteorological Administration, School

9 of Atmospheric Physics, Nanjing University of Information Science & Technology, Nanjing

10 210044, China

11 [2] State Key Laboratory of Remote Sensing Science, College of Global Change and Earth System

12 Science, Beijing Normal University, Beijing 100875, China

13 [3] Earth System Science Interdisciplinary Center, Department of Atmospheric and Oceanic Science,

14 University of Maryland, College Park, MD, USA

15 [4] State Key Laboratory of Atmospheric Boundary Layer Physics and Atmospheric Chemistry,

16 Institute of Atmospheric Physics, Chinese Academy of Sciences, Beijing, 100029, China

17

18 Correspondence to: Yuying Wang (yuyingwang@nuist.edu.cn)

19 **Abstract**. In this study, the mixing state of size-resolved soot particles and their influencing factors

20 were investigated based on a five-month aerosol volatility measurement at a suburban site (Xingtai,

21 XT) in the central North China Plain (NCP). The volatility and mixing state of soot particles at XT

22 were complex caused by multiple pollution sources and various aging processes. The results suggest

23 that anthropogenic emissions can weaken the volatility of soot particles and enhance their degree of

24 external mixing. There were fewer externally mixed soot particles in warm months (June, July, and

25 August) than in cold months (May, September, and October). Monthly variations in the mean

26 coating depth ($D_{c,mean}$) of volatile matter on soot particles showed that the coating effect was stronger

27 in warm months than in cold months, even though aerosol pollution was heavier in cold months.

28 Moreover, the volatility was stronger, and the degree of internal mixing was higher in nucleation-

29 mode soot particles than in accumulation-mode soot particles. Relationships between $D_{c,mean}$ and

30 possible influencing factors [temperature (T), relative humidity (RH), and particulate matter with

31 diameters ranging from 10 to 400 nm] further suggest that high ambient T and RH in a polluted

32 environment could promote the coating growth of accumulation-mode soot particles. However, high

33 ambient T but low RH in a clean environment were beneficial to the coating growth of nucleation-

34 mode soot particles. Our results highlight the diverse impact of anthropogenic emissions and aging

35 processes on the mixing state of soot particles in different modes, which should be considered

36 separately in models to improve the simulation accuracy of aerosol absorption.

37

38 ## 1.   Introduction

39   Aerosols are mixed liquid and solid particles suspended in the atmosphere. Some aerosols are

40 directly produced from natural or anthropogenic sources (i.e., primary aerosols), and the rest are

41 indirectly transformed from gas precursors through atmospheric chemical reactions (i.e., secondary

42 aerosols). The newly formed particles can grow or shrink through various aging processes (e.g.,

43 condensation, coagulation, volatilization, chemical reactions). Aerosol physicochemical properties

44 (number concentration, shape, mixing state, optical properties, among others) are thus highly

45 variable. This is one of the reasons why aerosols are highly uncertain in climate change assessments

46 (Bond et al., 2013；Seinfeld et al., 2016; Bellouin et al., 2020; Christensen et al., 2021). Although

47 great efforts have been made to understand aerosol optical properties, the uncertainty of radiative

48 forcing caused by aerosols is still two to three times that of greenhouse gases (IPCC, 2021).

49   Aerosols can affect the earth-atmosphere radiation balance by scattering or absorbing shortwave

50 and longwave radiation, which is called the aerosol direct climate effect or aerosol-radiation

51 interactions. Many factors, such as aerosol chemical composition, mixing state, and ambient relative

52 humidity (RH), have complex impacts on aerosol-radiation interactions (e.g., Twohy et al., 2009;

53 Kuniyal and Guleria, 2019; Ren et al., 2021). According to the sixth IPCC report, the total direct

54   radiative forcing caused by anthropogenic aerosols is generally negative. However, light-absorbing

55   carbonaceous particles (LAC) have a warming effect on climate (Ramana et al., 2010; Gustafsson

56   and Ramanathan, 2016), which can partly offset the cooling effect caused by scattering aerosols,

57   such as sulfate. Black carbon (BC) is the most important LAC compound, mostly emitted as soot

58   from anthropogenic sources (incomplete fossil fuel combustion and biomass burning). Some

59   experiments have suggested that BC in urban polluted environments can play an important role in

60   pollution formation and development. The internal mixing of BC with secondly formed matter could

61   also greatly enhance light absorption (Peng et al., 2016; Zhou et al., 2017). However, studies on the

62   mixing state of BC or soot particles in the actual atmosphere are few due to limited observations.

63   Aerosol volatility refers to the shrinking extent of particles at a certain temperature. The mixing

64   state of soot particles is closely related to aerosol volatility at high temperatures (Philippin et al.,

65   2004; Wehner et al., 2009). This is because most primary soot particles from anthropogenic sources

66   are refractory, hydrophobic, and externally mixed. In a polluted environment, primary soot particles

67   are easily transformed to internally mixed particles through certain coating processes in the

68   atmosphere (Cheng et al., 2012; Peng et al., 2016; F. Zhang et al., 2020). However, coating matter

69   is generally non-refractory because most of the matter consists of secondary chemical species, such

70   as organics, sulfate, and nitrate (Philippin et al., 2004; Hong et al., 2017). This is why aerosol

71   volatility can characterize the mixing state of soot particles (Wehner et al., 2009; Hossain et al.,

72   2012; S. Zhang et al., 2016). A volatility tandem differential mobility analyzer (VTDMA) is usually

73   used to quantify aerosol volatility by measuring the change in particle size at a set temperature.

74   Aerosol volatility measured by a VTDMA at a high temperature (> 280ºC) can be used to study the

75   mixing state of soot particles (Philippin et al., 2004; Wehner et al., 2009; Y. Zhang et al., 2016;

76   Wang et al., 2017).

77   Over the past years, several studies have reported the volatility and mixing state of soot particles

78   based on VTDMA measurements in the North China Plain (NCP). For example, Wehner et al. (2009)

79   found that the mixing state of soot particles in Beijing and its surrounding region varied, especially

80   between new particle formation days and heavily polluted days. Using the same VTDMA and

81   aerosol optical data, Cheng et al. (2009) conducted an aerosol optical closure study, finding that soot

82   aging was rapid at the Yufa site south of Beijing. The coating on soot particles can enhance aerosol

83   absorption and scattering coefficients by a factor of 8 to 10 within several hours due to secondary

84   processing during the daytime, which is the combined effect of the increased thickness of the coating

85   shell and the transition of soot from an externally mixed state to a coated state. Cheng et al. (2012)

86   further indicated that aging and emissions were two competing factors in the mixing state of soot

87   particles. Based on VTDMA measurement data collected in 2015, Wang et al. (2017) indicated that

88   strict emission control measures implemented in Beijing and surrounding areas could enhance the

89　　volatility of soot particles and their degrees of external mixing. At another regional site (Xinghe) in

90　　the northern part of the NCP, S. Zhang et al. (2016) found that the mixing state of ambient particles

91　　was complex with different volatilities. Furthermore, Y. Zhang et al. (2016) suggested that the

92　　average shell-to-core ratio and absorption enhancement (E_{ab}) of ambient BC was 2.1–2.7 and 1.6–

93　　1.9, respectively.

94　　　These studies imply that anthropogenic emissions play an important role in the volatility and

95　　mixing sate of soot particles and that the coating on soot particles can greatly enhance aerosol

96　　absorption. However, these studies were based on data collected during short-term observational

97　　periods in the northern part of the NCP. Recent studies (Y. Wang et al., 2018, 2019, 2021) have

98　　shown that anthropogenic sources and aerosol aging processes are various in the north and central-

99　　south NCP, leading to diverse aerosol physiochemical properties between these regions in different

100　　seasons. More research about the volatility and mixing state of soot particles in the central-south

101　　NCP is needed to improve the accuracy of modeled aerosol optical properties.

102　　　This study investigates for the first time the volatility and mixing state of soot particles in the

103　　warm and cold seasons based on one comprehensive field campaign that took place in the central

104　　NCP, lasting five months. Exploring factors influencing the volatility and mixing state of soot

105　　particles in this study will improve the accuracy of modeled aerosol optical properties in the central

106　　NCP. This paper is organized as follows. Section 2 introduces the sampling site, instruments, and

107　　data analysis. Section 3 presents the results and discussion, including meteorological conditions,

108　　aerosol pollution levels, changes in volatility and mixing state of soot particles, and their influencing

109　　factors. Section 4 gives conclusions and summarizes the study.

110

2.　　Sampling site, instruments, and data analysis

2.1　　Sampling site

113　　　Data used in this study were collected at the National Meteorological Basic Station (37°11'N,

114　　114°22'E, 180 m above sea level) in Xingtai (XT), China, equipped with a variety of meteorological

115　　observation instruments. Y. Wang et al. (2018) reported that this site is located in a polluted area of

116　　the central-south NCP, influenced by multiple anthropogenic sources, such as industrial coal firing,

117　　fossil-fuel burning, agricultural activities, and household emissions. The long-distance transport of

118　　pollutants also influences the air quality at XT. Previous studies have suggested that air pollution at

119　　XT represents well regional pollution characteristics in the central NCP east of the Taihang

120　　Mountains (Y. Zhang et al., 2018; Y. Wang et al., 2018). A comprehensive field campaign named

121　　the Atmosphere-Aerosol-Boundary layer-Cloud (A^{2}BC) Interaction Joint Experiment was carried

122　　out at XT from May to October of 2016. Y. Wang et al. (2018) and Li et al. (2019) provide details

123　　about the XT site and the A^{2}BC campaign. Here, over five months of aerosol observational data,

124   including particle number size distribution (PNSD), aerosol volatility, and BC mass concentration,

125   were used to analyze the volatility and mixing state of soot particles and their influencing factors.

126

127   2.2   Instruments

128   2.2.1   Measuring PNSD and aerosol volatility

129   The tandem differential mobility analyzer (TDMA) system is widely used to measure the change

130   in particle size under special conditions, e.g., high humidity, high temperature, and chamber

131   chemical reactions (Swietlicki et al., 2008). In this campaign, the VTDMA system was used to

132   measure aerosol volatility at 300ºC. The inlet air sample was first dried by a Nafion^{TM} dryer to low

133   RH (< 30%), then neutralized by a soft X-ray neutralizer (model 3088, TSI Inc.; Fig. 1a). Afterwards,

134   quasi-monodisperse aerosols (Fig. 1b) with a certain dried diameter (D_d) were split by the first

135   differential mobility analyzer (DMA1). In this campaign, D_d was set to 40, 80, 110, 150, 200, and

136   300 nm. An automated valve located after the DMA1 had two outlet lines. Line 1 directly accessed

137   the water-based condensation particle counter (WCPC, model 3787, TSI Inc.), measuring the PNSD

138   of particle sizes ranging from 10 to 400 nm. Line 2 accessed a heating tube, vaporizing volatile

139   materials at a controlled high temperature (300ºC in this study). The ratio of particle size after

140   volatilization [$D_p(T)$] to D_d is defined as the aerosol shrink factor (i.e., $SF = D_p(T) / D_d$). After

141   heating, residual aerosols were generally polydisperse nonvolatile particles (Fig. 1c). The second

142   DMA (DMA2) and WCPC were used to measure the number size distribution of nonvolatile

143   particles, measuring the distribution function of SF (SF-MDF). Finally, the probability density

144   function of SF (SF-PDF) was retrieved using the TDMAfit algorithm (Stolzenburg and McMurry,

145   1988; Stolzenburg and McMurry, 2008).

146   In this study, we assume that the shape of all particles follows the core-shell model (nonvolatile

147   core and volatile shell; Fig. 1b). Residual particles after volatilization have different-sized

148   nonvolatile cores (Fig. 1c). Previous studies have suggested that residual particles at 300ºC mainly

149   consist of soot (Philippin et al., 2004; Wehner et al., 2009). Aerosol volatility measured by the

150   VTDMA in this study can thus reflect the degree of mixing state of soot particles.

151
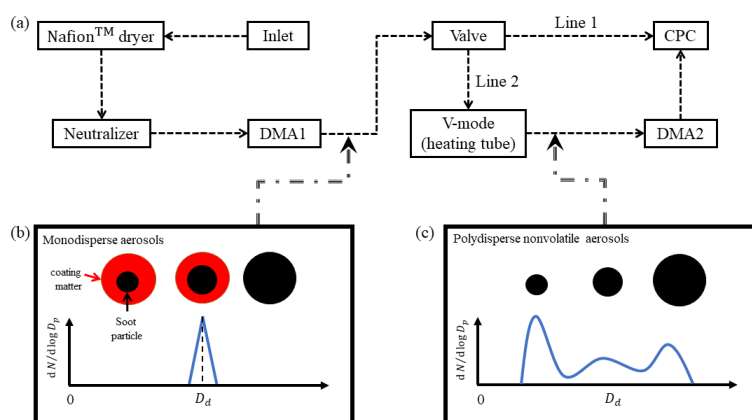
Figure 1. Schematic diagram of the volatility tandem differential mobility analyzer used in this study.

2.2.2 Measuring BC

BC aerosols are mainly emitted from incomplete combustion of carbon-containing fuels, including vehicle exhaust, coal, and biomasses (Novakov et al., 2003). In this campaign, a seven-wavelength aethalometer (model AE-33, Magee Scientific Corp.) was used to measure the mass concentration of BC (M_{BC}). After calibration, the sampling flow rate of the AE-33 was 5.0 L min^{-1}. A cyclone with particulate matter (diameters = 2.5 μm, or PM$_{2.5}$) was used in the sample inlet. Aerosol particles were collected on filter tape through a spot, and the instantaneous concentration of optically absorbing aerosols was retrieved from the rate of change of the attenuation of light transmitted through the filter. The wavelength channels of the AE-33 were 370, 470, 525, 590, 660, 880, and 940 nm. According to the manufacturer's instructions, data in channel 6 (i.e., 880 nm) can be used to retrieve M_{BC}.

2.2.3 VTDMA data analysis

The retrieved SF-PDF ($c(D_{\mathrm{d}}, SF)$) is normalized as $\int c(D_{\mathrm{d}}, SF)\,\mathrm{d}SF = 1$. The ensemble mean shrink factor (SF_{mean}) is then calculated as

$$SF_{\mathrm{mean}}(D_{\mathrm{d}}) = \int_0^\infty SF \cdot c(D_{\mathrm{d}}, SF)\mathrm{d}SF \ . \qquad (1)$$

Particles can be classified into several volatile groups according to different SF ranges (Y. Wang et al., 2017). The number fraction (NF) for each volatile group with the SF boundary of [a, b] is calculated as

$$NF(D_{\mathrm{d}}) = \int_a^b c(D_{\mathrm{d}}, SF)\mathrm{d}SF \ . \qquad (2)$$

Based on the core-shell assumption, the coating depth (D_{c}) of soot particles is defined as the

177 depth of shell materials (i.e., shell depth). According to the definition of SF, D_c for the particle

178 (D_d, SF) can be calculated as

$$D_c(D_d, SF) = \frac{D_d}{2}(1 - SF). \qquad (3)$$

180 The ensemble mean D_c ($D_{c,mean}$) using the normalized SF-PDF data is then calculated as

$$D_{c,mean}(D_d) = \int_0^\infty D_c(D_d, SF) \cdot c(D_d, SF)\mathrm{d}SF \quad . \quad (4)$$

182

3. Results and discussion

3.1 Meteorological conditions and aerosol pollution levels

185   Figure 1a-b shows the time series of ambient temperature (T), RH, and wind direction and

186 speed (WD and WS, respectively) during the campaign. Monthly changes in T are clearly seen (Fig.

187 2a). Average Ts in warm (June, July, and August) and cold (May, September, and October) months

188 were 25.73±3.80 and 19.0±5.74ºC, respectively. Figure 2a also suggests that RH was higher in July

189 and August than in other months.

190   Figure 2b shows that the wind changed significantly in different months at XT. Monthly wind

191 rose diagrams (Fig. S1) indicate that northwest winds prevailed in all months, likely caused by the

192 special terrain around XT (Y. Zhang et al., 2018). In July, weak southeast winds were also prevalent,

193 beneficial to the accumulation of air pollutants due to the stable atmospheric environment. In August,

194 the other prevailing wind was from the north, always strong and beneficial for atmospheric diffusion.

195
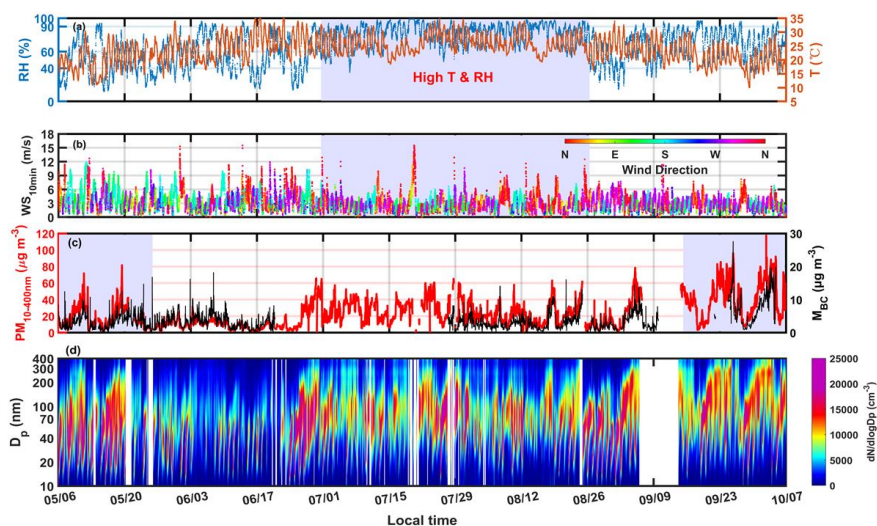
Figure 2. Time series of (**a**) ambient relative humidity (RH; unit: %) and temperature (T; unit: ºC), (**b**) wind direction (WD) and 10-minute-averaged wind speed (WS; unit: m s^{-1}), (**c**) mass

199 concentration of 10–400 nm particles (PM$_{10-400}$, in red; unit: μg m^{-3}), assuming that the aerosol

200 density is 1.6 g cm^{-3}, and mass concentration of black carbon (M_{BC}, in black; unit: μg m^{-3}), and (**d**)

201 particle number size distribution at the Xingtai site from 6 May 2016 to 6 October 2016.

202

203   In this study, the total mass concentration of 10–400-nm particles (PM$_{10-400}$) (Fig. 2c) was

204 calculated using PNSD data (Fig. 2d), assuming that the aerosol density was 1.6 g cm^{-3}. The average

205 PM$_{10-400}$ concentrations in warm and cold months were 19.68 ± 13.58 and 29.79 ± 21.37 μg m^{-3},

206 respectively, indicating much higher aerosol pollution in cold months than in warm months. In cold

207 months, PM$_{10-400}$ accumulated periodically as accumulation-mode ($D_p > 100$ nm) particles increased.

208 This is closely related to cyclic changes in general atmospheric circulation, reflected by the cycle of

209 winds (Fig. 2b). However, PM$_{10-400}$ was lower in May than in September and October, likely due to

210 the weaker particle growth in May. During warm months, PM$_{10-400}$ reached its lowest value in June

211 with the lowest number concentration of accumulation-mode particles of all months (Fig. S2),

212 suggesting that meteorological conditions in June were not conducive to particle growth. The high

213 T and RH in July and August were beneficial to particle growth by promoting atmospheric

214 photochemical and liquid chemical reactions (Z. Wu et al., 2018; Peng et al., 2021). Figure 2c

215 suggests that PM$_{10-400}$ was much higher in July and August than in June, although the mass

216 concentrations of black carbon (M_{BC}s) in these months were considerable. However, PM$_{10-400}$ was

217 lower in August than in July, likely because of the better atmospheric diffusion conditions in August.

218 Figure 2c also shows that changes in M_{BC} and PM$_{10-400}$ were similar, suggesting the non-trivial role

219 of BC in the formation processes of aerosol pollution. Recently, F. Zhang et al. (2020) demonstrated

220 that BC-catalyzed sulfate formation involving NO$_2$ and NH$_3$ plays an important role in the formation

221 of haze events.

222   In summary, during the field campaign, meteorological conditions varied. Changes in

223 meteorological parameters could influence the aging processes of particles, generating different

224 aerosol pollution levels in different months. These changes would have a large impact on the

225 volatility and mixing state of soot particles.

226

227 3.2   Monthly and diurnal variations in *SF*-PDF

228   Figure 3 shows wavelength-dependent, size-resolved mean *SF*-PDFs at XT. In general, *SF*-

229 PDFs had three peak modes, namely, at $SF \approx 0.4$ [very volatile (VV) mode], 0.6 [slightly volatile

230 (SV) mode], and 0.9 [nonvolatile (NV) mode]. The trimodal distributions of *SF*-PDFs at XT in the

231 central NCP differ from those at sites in the northern NCP (S. Zhang et al., 2016; Y. Wang et al.,

232 2017), implying highly complex volatility and mixing state of soot particles at XT. Note that the

233 *SF*-PDF of 40-nm particles has a quasi-unimodal distribution pattern, with low fractions of NV-

Atmospheric
Chemistry
and Physics
Discussions

Open Access

EGU

234 and SV-mode particles. Previous studies have indicated that most NV-mode particles are

235 externally mixed soot particles (Cheng et al., 2012; Cheung et al., 2016). This suggests that soot

236 particles in nucleation mode (represented by 40-nm particles) in this study had strong volatility

237 and a high degree of internal mixing. Figure 3 also suggests that the fraction of NV-mode particles

238 increased with increasing particle size, indicating a higher fraction of externally mixed soot

239 particles in accumulation mode. This is related to the primary size of soot particles. Levy et al.

240 (2014) and Wu et al. (2017) have suggested that freshly emitted refractory particles (like BC) are

241 primarily in accumulation mode.

242
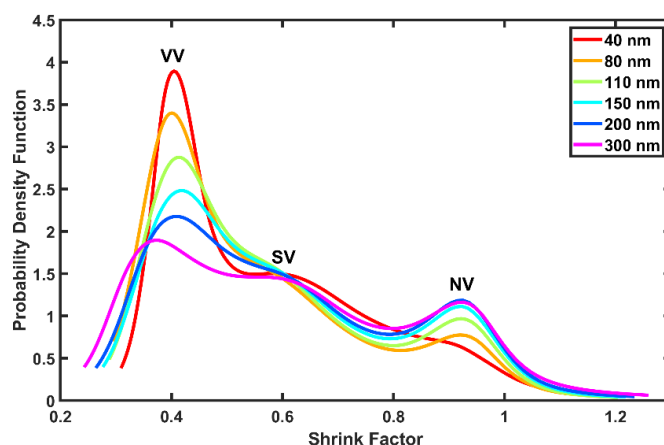
243
244 **Figure 3.** Size-resolved mean probability density functions of the shrink factor at different
245 wavelenghts. VV stands for "very volatile", SV stands for "slightly volatile", and NV stands for
246 "non-volative".

247

248 Figure 4a-b shows that VV-mode fractions in the *SF*-PDFs of 40-nm and 80-nm particles were

249 higher in warm months than in cold months, indicating that nucleation-mode soot particles were

250 more volatile in warm months. Our previous study has shown that new particle formation (NPF)

251 events occurred frequently at XT (Y. Wang et al., 2018). Wehner et al. (2009) reported that most

252 newly formed matter is composed of organics and sulfate, easily volatized at 300ºC. All this implies

253 that coating by newly formed secondary matter was the possible reason for the high volatility of

254 nucleation-mode soot particles in warm months. For accumulation-mode (110–300 nm) particles

255 (Fig. 4c-f), monthly changes in *SF*-PDF patterns are clearly seen. In general, *SF* peak values of the

256 VV mode were smaller (meaning a thicker coating of volatile matter), and fractions of VV-mode

257 particles were higher in warm months (especially in July) than in cold months, indicating that the

258 coating on accumulation-mode soot particles was also stronger in warm months than in cold months.

259 As previously mentioned, meteorological conditions in warm months (i.e., high *T* and RH) were

260   favorable to the particle growth of soot particles through atmospheric photochemical and liquid

261   chemical reactions. In cold months (May, September, and October), the volatility of accumulation-

262   mode soot particles was relatively lower, indicating thinner coating matter on the surfaces of soot

263   particles in the polluted cold environment. This is consistent with measurements made at an urban
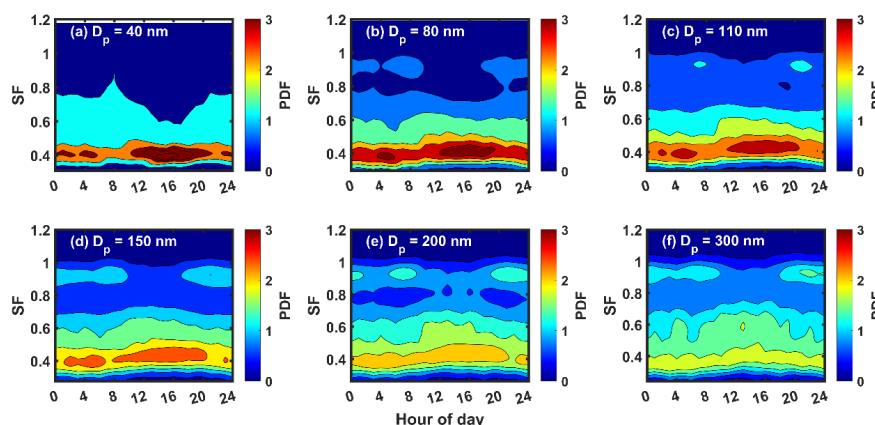
264   site in Beijing (Y. Wang et al., 2017).

265
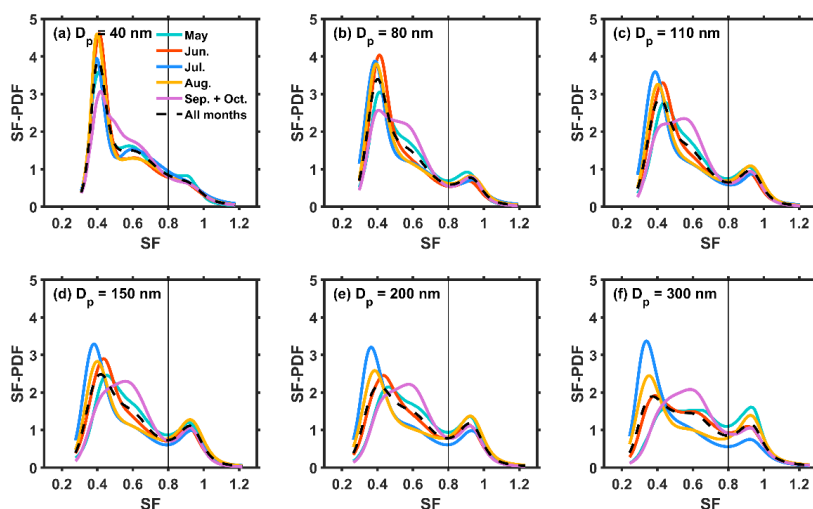
Figure 4. Monthly variations in the mean shrink factor (*SF*) probability distribution functions (*SF*-PDFs) for particles with diameters of (a) 40 nm, (b) 80 nm, (c) 110 nm, (d) 150 nm, (e) 200 nm, and (f) 300 nm.

271   Figure 5 shows diurnal variations in *SF*-PDF for different size particles, illustrating the distinct

272   diurnal variation patterns of *SF*-PDF for nucleation- and accumulation-mode particles. VV-mode

273   fractions for 40-nm and 80-nm particles (~*SF* = 0.4) increased sharply from around noon into the

274   afternoon (Fig. 5a-b). Figure S3 shows that the number concentration of 40-nm and 80-nm particles

275   increased quickly due to the influence of NPF events. This further corroborates that newly formed

276   particles created during NPF events are the possible coating matter on nucleation-mode soot

277   particles. Figure 5c-f suggests that NV-mode fractions in accumulation-mode soot particles (~*SF* =

278   0.9) were higher than those in nucleation-mode soot particles and that these fractions became higher

279   with increasing particle size. NV-mode fractions in accumulation-mode soot particles clearly

280   increased during the morning and evening rush hours. This suggests that anthropogenic emissions

281   have a large impact on the volatility and mixing state of soot particles, especially for accumulation-

282   mode soot particles. Previous studies have shown that some of the primary pollutants generated by

283   human activities are composed of refractory materials, such as BC (Philippin et al., 2004; Levy et

284   al., 2014). An increase in primary refractory particles could weaken the ensemble volatility and

285   mixing state of soot particles. Figure 3c-f also shows that the NV-mode fraction in the *SF*-PDF of

286   accumulation-mode particles decreased sharply in the daytime, likely caused by the coating effect

287   of volatile matter through photochemical reactions.

288

289

290   **Figure 5.** Diurnal variations in size-resolved shrink factor (*SF*) probability distribution functions

291   (PDFs) for particles with diameters of (a) 40 nm, (b) 80 nm, (c) 110 nm, (d) 150 nm, (e) 200 nm,

292   and (f) 300 nm.

293

294   In summary, the volatility and mixing state of soot particles were complex at XT during the

295   field campaign. Soot particles in the nucleation mode had strong volatility and a high degree of

296   internal mixing, likely due to the impact of frequent NPF events that occurred during this campaign.

297   The strong volatility and high degree of internal mixing in warm months were likely caused by the

298   aging processes of particles. Anthropogenic emissions also had a large impact on the volatility and

299   mixing state of soot particles, especially in the accumulation mode. The impacts of anthropogenic

300   emissions and secondary chemical reactions on the volatility and mixing state of soot particles will

301   be further discussed next.

302

303   3.3   Factors influencing the volatility and mixing state of soot particles

304   3.3.1   The impact of anthropogenic emissions on the volatility and mixing state of soot

305   particles

306   As previously discussed, soot particles from anthropogenic emissions were always refractory

307   and nonvolatile at 300°C. Analyzing the relationship between the number fraction of nonvolatile-

308   mode particles (NF_{NV}, $SF > 0.8$) in *SF*-PDFs and M_{BC} can verify this because BC is the main matter

309   in soot particles. Figure 6a shows that NF_{NV} reached two peak values, one during the morning rush

310   hour at about 08:00 and the other during the evening rush hour at about 20:00. M_{BC} also reached

311   two peak values at those same times (Fig. 6b). Overall, the diurnal variation trends of NF_{NV} for all

312   sizes and M_{BC} were similar. This suggests the great impact of anthropogenic BC on the volatility

313   and mixing state of soot particles. NF_{NV} decreased quickly after rush hours, especially in the

314   morning (Fig. 6a), suggesting that the aging processes of primary soot particles were quick at this

315   heavily polluted site.

316
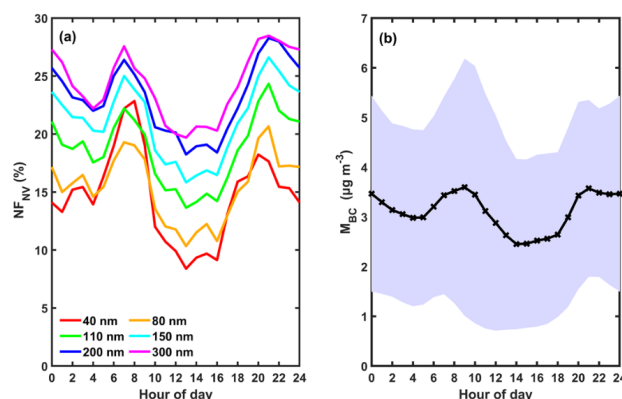
317

318   **Figure 6**. Diurnal variations in (**a**) wavelength-dependent, size-resolved number fractions of

319   nonvolatile particles (NF_{NV}), and (**b**) mass concentration of black carbon (M_{BC}). The purple,

320   shaded area shows the standard deviations of M_{BC}.

321

322   3.3.2   The impact of aging processes on the volatility and mixing state of soot particles

323   Lower SF_{mean} values mean stronger aerosol volatility, indicating a larger coating depth of volatile

324   matter on soot particles. Figure 7a suggests that volatility is stronger during daytime than at night

325   (i.e., a lower SF_{mean}), particularly for 40-nm particles. This illustrates the large impact of

326   photochemical reactions on the volatility and mixing state of soot particles. The SF_{mean} of 80-nm

327   particles was lower than that of 40-nm particles, meaning that the volatility of nucleation-mode soot

328   particles became larger with increasing particle size. Inversely, SF_{mean} increased with increasing

329   particle size in the accumulation mode (110–300 nm), suggesting weaker volatility and a smaller

330   coating depth for larger accumulation-mode soot particles.

331

332
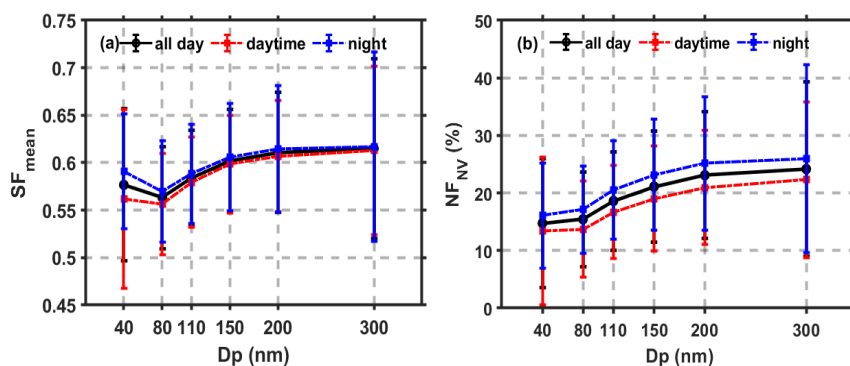
Figure 7. (**a**) Size-resolved ensemble mean shrink factors (SF_{mean}) and (**b**) size-resolved number fractions of nonvolatile particles (NF_{NV}) during the 24-hr day (black solid lines), during daytime (red dotted lines), and during nighttime (blue dotted lines). The error bars denote standard deviations.

Figure 8 shows the diurnal variation in SF_{mean} in different months for different particle sizes. Figure 8a-b shows that the SF_{mean} of 40-nm and 80-nm particles clearly increased during the morning and evening rush hours in all months. However, the SF_{mean} of 40-nm and 80-nm particles decreased sharply in the afternoon. This suggests that the volatility of nucleation-mode soot particles was easily influenced by anthropogenic emissions during rush hours and photochemical reactions in the daytime. The diurnal variation patterns of SF_{mean} (Fig. 8c-f) in the accumulation mode were diverse in different months. The SF_{mean} in warm months was usually lower than in cold months, indicating a larger impact of aging processes on the volatility of accumulation-mode soot particles in warm months. Figure 8c-f also shows that the SF_{mean} in accumulation mode was lowest in July. This suggests that high T, high RH, and the stable atmospheric environment in July were conducive to the coating of secondary matter on accumulation-mode soot particles, a possible reason for the high aerosol pollution levels in July. Moreover, Fig. 8 suggests that monthly variations in SF_{mean} became larger with increasing particle size. The seasonal variation in the coating effect should thus be considered when modeling physicochemical properties of soot particles, especially larger particles.

To further investigate the impact of aging processes on the mixing state of soot particles, size-resolved NF_{NV} in the daytime and at night were compared (Fig. 7b). NF_{NV} was always lower in the daytime than at night, meaning that the fraction of externally mixed soot particles in the daytime was lower. This further indicates that photochemical reactions in the daytime can transform externally mixed soot particles into internally mixed soot particles. Figure 7b also shows that NF_{NV} increased with increasing particle size, meaning a higher degree of external mixing of larger particles. This suggests that the degree of external mixing was higher for accumulation-mode soot particles than nucleation-mode particles.

359   The diurnal variation patterns of NF_{NV} (Fig. S4) and SF_{mean} (Fig. 8) in different months were

360   similar. Externally mixed soot particles increased during the morning and evening rush hours due

361   to enhanced anthropogenic emissions. Monthly differences in NF_{NV} increased with increasing

362   particle size. Figure S4 also shows a lower number fraction of externally mixed soot particles (i.e.,

363   a smaller NF_{NV}) in warm months than in cold months.

364   These results illustrate the distinct volatilities and mixing states of soot particles between the

365   nucleation and accumulation modes. A lower degree of external mixing and thicker coating depth

366   in nucleation-mode particles exists. It is thus important to quantify the impact of the coating effect

367   for nucleation-mode soot particles when studying aerosol physicochemical properties. The next

368   section analyzes the coating depth and its influencing factors.

369
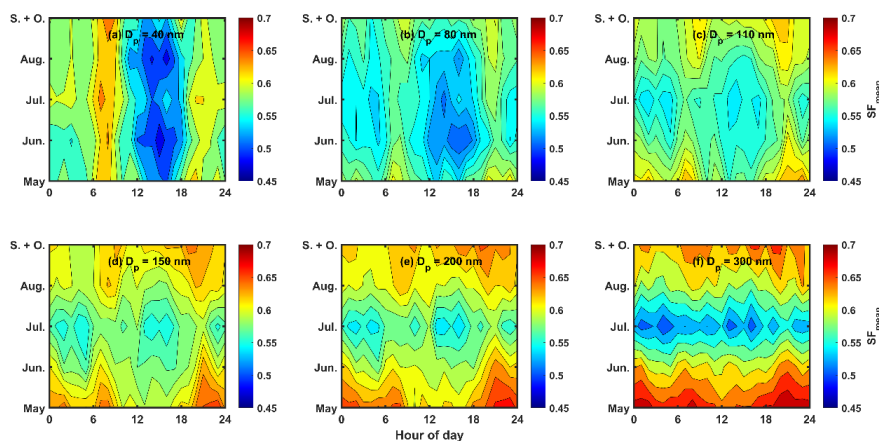
371   **Figure 8**. Diurnal variations in ensemble mean shrink factor (SF_{mean}) in different months for
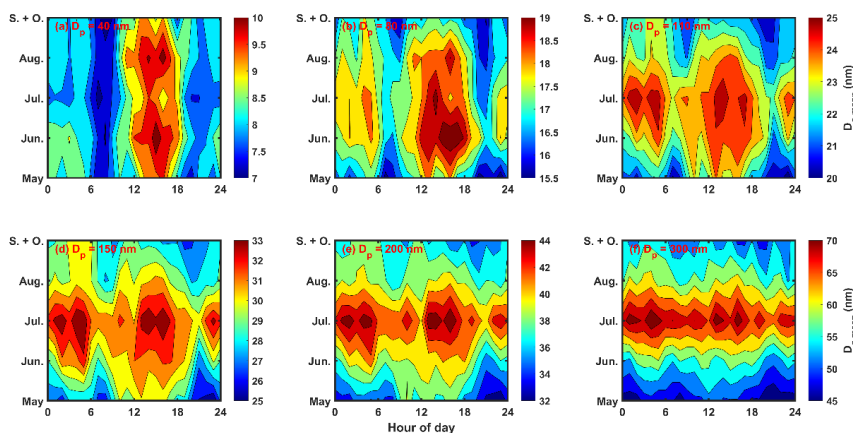
372   different particle sizes.

373

374   3.4   The coating depth of secondary matter on soot particles

375   The ensemble mean coating depth on soot particles ($D_{c,mean}$) can be calculated using Eq. (4).

376   Figure 9 shows diurnal variations in $D_{c,mean}$ in different months for different particle sizes. The

377   diurnal variation patterns of $D_{c,mean}$ for nucleation-mode and accumulation-mode soot particles

378   differ greatly. The diurnal variation patterns of $D_{c,mean}$ in different months were similar for

379   nucleation-mode soot particles (40-nm and 80-nm particles) but not for accumulation-mode soot

380   particles (110–300-nm particles). The enhancement of $D_{c,mean}$ in the daytime occurred in all months

381   for nucleation-mode soot particles but only in the warm months for accumulation-mode soot

382   particles. At night, the enhancement of $D_{c,mean}$ for accumulation-mode soot particles was strong,

383   especially in warm months. However, it was weak for nucleation-mode soot particles. These all

384 imply large differences in $D_{c,mean}$ in different months for nucleation-mode and accumulation-mode

385 soot particles, likely caused by variations in meteorological conditions and aerosol pollution levels.

386

387

388 **Figure 9**. Diurnal variations in ensemble mean coating depth ($D_{c,mean}$) on soot particles in different

389 months for different particle sizes. Note that the color bars have different ranges of values in each

390 panel.

391

392 The relationships between $D_{c,mean}$ and several possible influencing factors (T, RH, and PM$_{10\text{-}}$

393 $_{400nm}$) were further analyzed (Fig. 10). Figures 10a and 10d show positive correlations between

394 $D_{c,mean}$ and T for both nucleation-mode and accumulation-mode particles (represented by 40-nm and

395 300-nm particles, respectively). This is consistent with the results shown in Fig. 7. The high daytime

396 T was conducive to the aging of soot particles likely caused by strong photochemical reactions.

397 However, the relationships between RH and $D_{c,mean}$ (Figs. 9b and 9e) and between PM$_{10\text{-}400nm}$ and

398 $D_{c,mean}$ (Figs. 9c and 9f) were inverse between nucleation- and accumulation-mode soot particles.

399 $D_{c,mean}$ in the nucleation mode decreased with increasing RH and PM$_{10\text{-}400nm}$ for nucleation-

400 mode soot particles (Fig. 9b-c). This suggests that high ambient RH and severe aerosol pollution

401 events could inhibit the coating of nucleation-mode soot particles. Previous studies have reported

402 that aerosol pollution events were generally associated with high RH in the NCP (G. Wang et al.,

403 2016; Z. Wu et al., 2018). This suggests that highly polluted environments with high ambient RH

404 are not beneficial to the formation of new particles, leading to the weak coating on nucleation-mode

405 soot particles. However, $D_{c,mean}$ in the accumulation mode increased with increasing RH and PM$_{10\text{-}}$

406 $_{400nm}$ (Fig. 9e-f). This suggests that highly polluted environments with high ambient RH favor the

407 growth of accumulation-mode soot particles by coating. This is possibly related to enhanced liquid-

408 phase chemical reactions under these environmental conditions. Considering that accumulation-

409 mode particles are the dominant components of PM$_{10\text{-}400nm}$, this further implies that the coating on

410   soot particles is important to the formation of heavy aerosol pollution events.

411   In summary, high ambient T and RH levels appeared to promote the coating growth of

412   accumulation-mode soot particles in highly polluted environments. High ambient T but low RH

413   were beneficial to the coating growth of nucleation-mode soot particles in less polluted

414   environments.

415
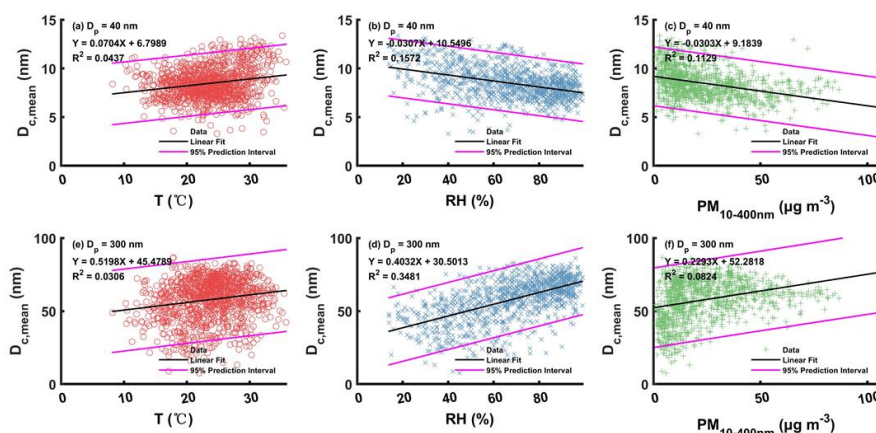
416

417   **Figure 10**. Relationships between ensemble mean coating depth ($D_{c,mean}$) and ambient T (a, d) and

418   RH (b, e), and $PM_{10\text{-}400nm}$ (c, f) for 40-nm (top panels) and 300-nm (bottom panels) particles. Black

419   lines show the linear best-fit lines through the data, and magenta lines show the 95% prediction

420   levels. Linear best-fit relations and coefficients of determination are given in each panel.

421

4.   Summary and conclusions

423   Soot particles containing most of the black carbon (BC) in the atmosphere are the most

424   important light-absorbing carbonaceous particles. Investigating the mixing state of soot particles in

425   the field is crucial to accurately model aerosol absorption and reduce the uncertainty of radiative

426   forcing caused by aerosols in climate models.

427   Here, over five months of volatility tandem differential mobility analyzer (VTDMA) data

428   collected at a heavily polluted suburban site (Xingtai, or XT) from May to October of 2016 were

429   used to study the volatility and mixing state of size-resolved soot particles and their influencing

430   factors. Ambient meteorological variables [temperature (T), relative humidity (RH), and winds]

431   varied between the warm (June, July, and August) and cold (May, September, and October) months

432   of the field campaign. Variations in meteorological parameters could induce various aerosol aging

433   processes and different levels of aerosol pollution, largely impacting the volatility and mixing state

434   of soot particles.

Atmospheric
Chemistry
and Physics
Discussions

Open Access

EGU

435   The retrieved probability density function of the shrink factor (SF-PDF) at XT had three modes,

436   demonstrating that the volatility and mixing state of soot particles were more complex at XT than

437   at other sites in the North China Plain. Compared with accumulation-mode soot particles,

438   nucleation-mode soot particles were more volatile and had a higher degree of internal mixing. The

439   diurnal variation patterns of SF-PDFs suggest that coating by newly formed particles was the

440   possible reason for the enhanced volatility of nucleation-mode soot particles in the daytime.

441   Moreover, enhanced nocturnal liquid chemical reactions were responsible for the enhanced

442   volatility of accumulation-mode soot particles in the nighttime. The ensemble mean SF (SF_{mean}) was

443   size dependent and varied monthly. The monthly variations in SF_{mean} became larger with increasing

444   particle size, implying a stronger seasonal variation of the coating effect on soot particles for larger-

445   sized particles.

446   The similar diurnal variation trends of the number fraction of nonvolatile mode particles (NF_{NV})

447   in SF-PDFs and the mass concentration of BC (M_{BC}) suggest that human activities had a negative

448   influence on the volatility and degree of internal mixing of soot particles, especially for

449   accumulation-mode soot particles. In general, less externally mixed soot particles (i.e., a smaller

450   NF_{NV}) were present in warm months than in cold months. NF_{NV} was always lower in the daytime

451   than at night, suggesting a lower fraction of externally mixed soot particles in the daytime. This

452   suggests that daytime photochemical reactions may promote the transformation of externally mixed

453   soot particles into internally mixed soot particles. Moreover, NF_{NV} increased with increasing particle

454   size, meaning a higher degree of external mixing for larger-sized particles. This also suggests that

455   the degree of external mixing was higher for accumulation-mode soot particles than for nucleation-

456   mode soot particles.

457   To explore factors influencing soot-particle volatility and mixing state, the ensemble mean

458   coating depth ($D_{c,mean}$) of volatile matter on soot particles was investigated. $D_{c,mean}$ was thicker in

459   warm months than in cold months, even though aerosol pollution was heavier in cold months. In

460   warm months, $D_{c,mean}$ was larger in July than in other months, likely because high T, high RH, and

461   the stable atmospheric environment in July were conducive to the coating effect on soot particles.

462   The relationships between $D_{c,mean}$ and possible influencing factors (i.e., T, RH, and $PM_{10-400nm}$) show

463   that high ambient T and RH in a polluted environment promoted the coating growth of

464   accumulation-mode soot particles. High ambient T but low RH in a clean environment was

465   beneficial to the coating growth of nucleation-mode soot particles.

466   These results demonstrate great differences in the volatility and mixing state between nucleation-

467   and accumulation-mode soot particles. The impact of anthropogenic emissions on the volatility and

468   mixing state of soot particles was clearly seen, especially for accumulation-mode soot particles. The

469   monthly variations in meteorological conditions and aerosol pollution levels may induce different

470   aerosol aging processes, strongly impacting the volatility and mixing state of soot particles. This

471   study suggests that differences between the mixing states of nucleation- and accumulation-mode

472   soot particles and their influencing factors should be considered in climate models.

473

479

480   *Data availability.* The measurement data from the field experiment used in this study are available

481   from the first author upon request (yuyingwang@nuist.edu.cn).

482

483   *Author contributions.* YW conceived the study and led the overall scientific questions. YW,

484   RH, and QW processed the measurement data and prepared this paper. ZL, MC copyedited the

485   article. Other co-authors participated in the implementation of this experiment and the discussion

486   of this paper.

487

488   *Competing interests.* The authors declare that they have no conflict of interest.

489

490

491

References

493 Bellouin, N., Quaas, J., Gryspeerdt, E., Kinne, S., Stier, P., Watson-Parris, D., Boucher, O., Carslaw, K.
494   S., Christensen, M., Daniau, A. L., Dufresne, J. L., Feingold, G., Fiedler, S., Forster, P., Gettelman,
495   A., Haywood, J. M., Lohmann, U., Malavelle, F., Mauritsen, T., McCoy, D. T., Myhre, G.,
496   Mülmenstädt, J., Neubauer, D., Possner, A., Rugenstein, M., Sato, Y., Schulz, M., Schwartz, S. E.,
497   Sourdeval, O., Storelvmo, T., Toll, V., Winker, D., and Stevens, B.: Bounding global aerosol radiative
498   forcing of climate change, Rev. Geophys., 58, e2019R-e2660R, 2020.
499 Bond, T. C., Doherty, S. J., Fahey, D. W., Forster, P. M., Berntsen, T., DeAngelo, B. J., Flanner, M. G.,
500   Ghan, S., Kärcher, B., Koch, D., Kinne, S., Kondo, Y., Quinn, P. K., Sarofim, M. C., Schultz, M. G.,
501   Schulz, M., Venkataraman, C., Zhang, H., Zhang, S., Bellouin, N., Guttikunda, S. K., Hopke, P. K.,
502   Jacobson, M. Z., Kaiser, J. W., Klimont, Z., Lohmann, U., Schwarz, J. P., Shindell, D., Storelvmo, T.,
503   Warren, S. G., and Zender, C. S.: Bounding the role of black carbon in the climate system: A scientific
504   assessment, J. Geophys. Res. Atmos., 118, 5380-5552, https://doi.org/10.1002/jgrd.50171, 2013.

505   Cheng, Y. F., Berghof, M., Garland, R. M., Wiedensohler, A., Wehner, B., Müller, T., Su, H., Zhang, Y.
506   H., Achtert, P., Nowak, A., Pöschl, U., Zhu, T., Hu, M., and Zeng, L. M.: Influence of soot mixing
507   state on aerosol light absorption and single scattering albedo during air mass aging at a polluted
508   regional site in northeastern China, J. Geophys. Res. Atmos., 114, 2009.
509   Cheng, Y. F., Su, H., Rose, D., Gunthe, S. S., Berghof, M., Wehner, B., Achtert, P., Nowak, A.,
510   Takegawa, N., Kondo, Y., Shiraiwa, M., Gong, Y. G., Shao, M., Hu, M., Zhu, T., Zhang, Y. H.,
511   Carmichael, G. R., Wiedensohler, A., Andreae, M. O., and Pöschl, U.: Size-resolved measurement of
512   the mixing state of soot in the megacity Beijing, China: diurnal cycle, aging and parameterization,
513   Atmos. Chem. Phys., 12, 4477-4491, 2012.
514   Cheung, H. H., Tan, H., Xu, H., Li, F., Wu, C., Yu, J. Z., and Chan, C. K.: Measurements of non-volatile
515   aerosols with a VTDMA and their correlations with carbonaceous aerosols in Guangzhou, China,
516   Atmos. Chem. Phys., 16, 8431-8446, 2016.
517   Christensen, M., Gettelman, A., Cermak, J., Dagan, G., Diamond, M., Douglas, A., Feingold, G.,
518   Glassmeier, F., Goren, T., Grosvenor, D., Gryspeerdt, E., Kahn, R., Li, Z., Ma, P. L., Malavelle, F.,
519   McCoy, I., McCoy, D., McFarquhar, G., Mülmenstädt, J., Pal, S., Possner, A., Povey, A., Quaas, J.,
520   Rosenfeld, D., Schmidt, A., Schrödner, R., Sorooshian, A., Stier, P., Toll, V., Watson-Parris, D.,
521   Wood, R., Yang, M., and Yuan, T.: Opportunistic experiments to constrain aerosol effective radiative
522   forcing, Atmos. Chem. Phys. Discuss., 2021, 1-60, 2021.
523   Gustafsson, Ö., and Ramanathan, V.: Convergence on climate warming by black carbon aerosols, Proc.
524   Natl. Acad. Sci. U.S.A., 113, 4243, https://doi.org/10.1073/pnas.1603570113, 2016.
525   Hong, J., Äijälä, M., Häme, S. A. K., Hao, L., Duplissy, J., Heikkinen, L. M., Nie, W., Mikkilä, J.,
526   Kulmala, M., Prisle, N. L., Virtanen, A., Ehn, M., Paasonen, P., Worsnop, D. R., Riipinen, I., Petäjä,
527   T., and Kerminen, V. M.: Estimates of the organic aerosol volatility in a boreal forest using two
528   independent methods, Atmos. Chem. Phys., 17, 4387-4399, https://doi.org/10.5194/acp-17-4387-
529   2017, 2017.
530   Hossain, A. M. M. M., Park, S., Kim, J. S., and Park, K.: Volatility and mixing states of ultrafine particles
531   from biomass burning, J. Hazard. Mater., 205-206, 189-197, 2012.
532   IPCC: Climate change 2021: The Physical Science Basis, sixth assessment of the Inter-governmental
533   Panel on Climate Change, in press, 2021.
534   Kuniyal, J. C., and Guleria, R. P.: The current state of aerosol-radiation interactions: a mini review, J.
535   Aerosol Sci., 130, 45-54, 2019.
536   Levy, M. E., Zhang, R., Zheng, J., Tan, H., Wang, Y., Molina, L. T., Takahama, S., Russell, L. M., and
537   Li, G.: Measurements of submicron aerosols at the California–Mexico border during the Cal-Mex
538   2010 field campaign, Atmos. Environ., 88, 308-319, 2014.
539   Li, Z., Wang, Y., Guo, J., Zhao, C., Cribb, M. C., Dong, X., Fan, J., Gong, D., Huang, J., Jiang, M., Jiang,
540   Y., Lee, S. S., Li, H., Li, J., Liu, J., Qian, Y., Rosenfeld, D., Shan, S., Sun, Y., Wang, H., Xin, J., Yan,
541   X., Yang, X., Yang, X., Zhang, F., and Zheng, Y.: East Asian Study of Tropospheric Aerosols and
542   their Impact on Regional Clouds, Precipitation, and Climate (EAST-AIR$_{CPC}$), J. Geophys. Res.
543   Atmos., 124, 13,026-13,054, https://doi.org/10.1029/2019JD030758, 2019.
544   Novakov, T., Ramanathan, V., Hansen, J. E., Kirchstetter, T. W., Sato, M., Sinton, J. E., and Sathaye, J.
545   A.: Large historical changes of fossil-fuel black carbon aerosols, Geophys. Res. Lett., 30,
546   https://doi.org/10.1029/2002GL016345, 2003.
547   Peng, J., Hu, M., Guo, S., Du, Z., Zheng, J., Shang, D., Zamora, M. L., Zeng, L., Shao, M., and Wu, Y.:
548   Markedly enhanced absorption and direct radiative forcing of black carbon under polluted urban

549   environments, Proc. Natl. Acad. Sci. U.S.A., 113, 4266-4271, 2016.

550   Peng, J., Hu, M., Shang, D., Wu, Z., Du, Z., Tan, T., Wang, Y., Zhang, F., and Zhang, R.: Explosive

551   secondary aerosol formation during severe haze in the North China Plain, Environ. Sci. Technol., 55,

552   2189-2207, https://doi.org/10.1021/acs.est.0c07204, 2021.

553   Philippin, S., Wiedensohler, A., and Stratmann, F.: Measurements of non-volatile fractions of pollution

554   aerosols with an eight-tube volatility tandem differential mobility analyzer (VTDMA-8), J. Aerosol

555   Sci., 35, 185-203, https://doi.org/10.1016/j.jaerosci.2003.07.004, 2004.

556   Ramana, M. V., Ramanathan, V., Feng, Y., Yoon, S., Kim, S., Carmichael, G. R., and Schauer, J. J.:

557   Warming influenced by the ratio of black carbon to sulphate and the black-carbon source, Nat. Geosci.,

558   3, 542-545, https://doi.org/10.1038/ngeo918, 2010.

559   Ren, R., Li, Z., Yan, P., Wang, Y., Wu, H., Cribb, M., Wang, W., Jin, X., Li, Y., and Zhang, D.:

560   Measurement report: the effect of aerosol chemical composition on light scattering due to the

561   hygroscopic swelling effect, Atmos. Chem. Phys., 21, 9977-9994, 2021.

562   Seinfeld, J. H., Bretherton, C., Carslaw, K. S., Coe, H., DeMott, P. J., Dunlea, E. J., Feingold, G., Ghan,

563   S., Guenther, A. B., Kahn, R., Kraucunas, I., Kreidenweis, S. M., Molina, M. J., Nenes, A., Penner, J.

564   E., Prather, K. A., Ramanathan, V., Ramaswamy, V., Rasch, P. J., Ravishankara, A. R., Rosenfeld,

565   D., Stephens, G., and Wood, R.: Improving our fundamental understanding of the role of aerosol-

566   cloud interactions in the climate system, Proc. Natl. Acad. Sci. U.S.A., 113, 5781, 2016.

567   Stolzenburg, M. R., and McMurry, P. H.: TDMAFIT user's manual, University of Minnesota,

568   Department of Mechanical Engineering, Particle Technology Laboratory, Minneapolis, 1-61, 1988.

569   Stolzenburg, M. R., and McMurry, P. H.: Equations governing single and tandem DMA configurations

570   and a new lognormal approximation to the transfer function, Aerosol Sci. Tech., 42, 421-432, 2008.

571   Swietlicki, E., Hansson, H. C., Hämeri, K., Svenningsson, B., Massling, A., Mcfiggans, G., Mcmurry, P.

572   H., Petäjä, T., Tunved, P., Gysel, M., Topping, D., Weingartner, E., Baltensperger, U., Rissler, J.,

573   Wiedensohler, A., and Kulmala, M.: Hygroscopic properties of submicrometer atmospheric aerosol

574   particles measured with H-TDMA instruments in various environments—a review, Tellus B: Chem.

575   Phys. Meteor., 60, 432-469, https://doi.org/10.1111/j.1600-0889.2008.00350.x, 2008.

576   Twohy, C. H., Coakley Jr., J. A., and Tahnk, W. R.: Effect of changes in relative humidity on aerosol

577   scattering near clouds, J. Geophys. Res. Atmos., 114, 2009.

578   Wang, G., Zhang, R., Gomez, M. E., Yang, L., Zamora, M. L., Hu, M., Lin, Y., Peng, J., Guo, S., and

579   Meng, J.: Persistent sulfate formation from London Fog to Chinese haze, Proc. Natl. Acad. Sci. U.S.A.,

580   113, 13,630-13,635, 2016.

581   Wang, Y., Zhang, F., Li, Z., Tan, H., Xu, H., Ren, J., Zhao, J., Du, W., and Sun, Y.: Enhanced

582   hydrophobicity and volatility of submicron aerosols under severe emission control conditions in

583   Beijing, Atmos. Chem. Phys., 17, 5239-5251, https://doi.org/10.5194/acp-17-5239-2017, 2017.

584   Wang, Y., Li, Z., Zhang, Y., Du, W., Zhang, F., Tan, H., Xu, H., Fan, T., Jin, X., Fan, X., Dong, Z.,

585   Wang, Q., and Sun, Y.: Characterization of aerosol hygroscopicity, mixing state, and CCN activity at

586   a suburban site in the central North China Plain, Atmos. Chem. Phys., 18, 11,739-11,752,

587   https://doi.org/10.5194/acp-18-11739-2018, 2018.

588   Wang, Y., Li, Z., Zhang, R., Jin, X., Xu, W., Fan, X., Wu, H., Zhang, F., Sun, Y., Wang, Q., Cribb, M.,

589   and Hu, D.: Distinct ultrafine- and accumulation-mode particle properties in clean and polluted urban

590   environments, Geophys. Res. Lett., 46, 10,918-10,925, https://doi.org/10.1029/2019GL084047, 2019.

591   Wang, Y., Wang, J., Li, Z., Jin, X., Sun, Y., Cribb, M., Ren, R., Lv, M., Wang, Q., Gao, Y., Hu, R.,

592   Shang, Y., and Gong, W.: Contrasting aerosol growth potential in the northern and central-southern
593   regions of the North China Plain: implications for combating regional pollution, Atmos. Environ.,
594   267, 118723, https://doi.org/10.1016/j.atmosenv.2021.118723, 2021.
595 Wehner, B., Berghof, M., Cheng, Y. F., Achtert, P., Birmili, W., Nowak, A., Wiedensohler, A., Garland,
596   R. M., Pöschl, U., and Hu, M.: Mixing state of nonvolatile aerosol particle fractions and comparison
597   with light absorption in the polluted Beijing region, J. Geophys. Res. Atmos., 114, 85-86, 2009.
598 Wu, Y., Wang, X., Tao, J., Huang, R., Tian, P., Cao, J., Zhang, L., Ho, K. F., Han, Z., and Zhang, R.:
599   Size distribution and source of black carbon aerosol in urban Beijing during winter haze episodes,
600   Atmos. Chem. Phys., 17, 7965-7975, https://doi.org/10.5194/acp-17-7965-2017, 2017.
601 Wu, Z., Wang, Y., Tan, T., Zhu, Y., Li, M., Shang, D., Wang, H., Lu, K., Guo, S., Zeng, L., and Zhang,
602   Y.: Aerosol liquid water driven by anthropogenic inorganic salts: implying its key role in haze
603   formation over the North China Plain, Environ. Sci. Tech. Lett., 5, 160-166,
604   https://doi.org/10.1021/acs.estlett.8b00021, 2018.
605 Zhang, F., Wang, Y., Peng, J., Chen, L., Sun, Y., Duan, L., Ge, X., Li, Y., Zhao, J., Liu, C., Zhang, X.,
606   Zhang, G., Pan, Y., Wang, Y., Zhang, A. L., Ji, Y., Wang, G., Hu, M., Molina, M. J., and Zhang, R.:
607   An unexpected catalyst dominates formation and radiative forcing of regional haze, Proc. Natl. Acad.
608   Sci. U.S.A., 117, 3960, https://doi.org/10.1073/pnas.1919343117, 2020.
609 Zhang, S. L., Ma, N., Kecorius, S., Wang, P. C., Hu, M., Wang, Z. B., Größ, J., Wu, Z. J., and
610   Wiedensohler, A.: Mixing state of atmospheric particles over the North China Plain, Atmos. Environ.,
611   125, Part A, 152-164, https://doi.org/10.1016/j.atmosenv.2015.10.053, 2016.
612 Zhang, Y., Zhang, Q., Cheng, Y., Su, H., Kecorius, S., Wang, Z., Wu, Z., Hu, M., Zhu, T., Wiedensohler,
613   A., and He, K.: Measuring the morphology and density of internally mixed black carbon with SP2
614   and VTDMA: new insight into the absorption enhancement of black carbon in the atmosphere, Atmos.
615   Meas. Tech., 9, 1833-1843, https://doi.org/10.5194/amt-9-1833-2016, 2016.
616 Zhang, Y., Du, W., Wang, Y., Wang, Q., Wang, H., Zheng, H., Zhang, F., Shi, H., Bian, Y., Han, Y., Fu,
617   P., Canonaco, F., Prévôt, A. S. H., Zhu, T., Wang, P., Li, Z., and Sun, Y.: Aerosol chemistry and
618   particle growth events at an urban downwind site in North China Plain, Atmos. Chem. Phys., 18,
619   14,637-14,651, https://doi.org/10.5194/acp-18-14637-2018, 2018.
620 Zhou, C., Zhang, H., Zhao, S., and Li, J.: Simulated effects of internal mixing of anthropogenic aerosols
621   on the aerosol−radiation interaction and global temperature, Int. J. Climatol., 37, 972-986, 2017.
622